NANO LETTERS

pubs.acs.org/NanoLett Letter

On-Wire Halide Perovskite-Heterostructure-Based Photodetectors for Encrypted Communication

Qihang Lv, Xuyang Li, Zitong Xu, Xia Shen,* Kin Man Yu, Johnny C. Ho, and Pengfei Guo*

Cite This: *Nano Lett.* 2025, 25, 12091−12100 Read Online

ACCESS | Metrics & More | Article Recommendations | Supporting Information

ABSTRACT: All-inorganic lead halide perovskites have generated considerable research interest due to their distinctive electronic and optoelectronic properties. In particular, their inherently soft crystal lattice allows greater tolerance to lattice mismatch, offering promising opportunities for heterostructure formation. Here, we report on a synthesis strategy of the on-wire $CsPbCl_3$−$CsPbI_3$ heterostructure via a magnetic-pulling chemical vapor deposition approach. Microstructural characterization reveals the abrupt mutation of compositions along the axial direction of the wire. Microphotoluminescence mapping clearly shows dual-wavelength emissions at 417 and 698 nm at the heterointerface. Optical waveguide investigation indicates that the nanowires have asymmetric transmission characteristics. Additionally, photodetectors based on these heterostructures exhibit superior photoelectric performance, including high responsivity and high detectivity, which not only exhibit a remarkable image-sensing capability but also establish encrypted imaging for innovative applications. All of these findings highlight the potential of combining on-wire band-gap engineering with advanced image techniques, providing insights into the development of next-generation secure information communications.

KEYWORDS: *on-wire band-gap engineering, perovskite heterostructure nanowires, high-performance photodetection, encrypted imaging*

Semiconductor photodetectors play a crucial role in remote sensing, environmental monitoring, medical imaging, military fields, optical communications, and encrypted imaging.[1−8] Among them, the optical communication technology using specific wavelength lasers as optical signals and data information media have attracted considerable research interest in novel detection and encryption technologies due to their high confidentiality and security.[9−16] However, with the development of optical communication and encrypted imaging technology, the performance requirements of photodetectors in terms of on/off ratio, responsivity, sensitivity, and response time are also increasing.[17−23] Therefore, the preparation of high-quality semiconductor materials is essential for high-performance photodetectors.

In recent years, all-inorganic halide perovskite nanostructures have emerged as essential constituents in modern semiconductor materials for integrated photonics due to their high absorption coefficient, long carrier diffusion length, soft crystal lattice, and tunable band gap.[24−32] In particular, the exquisite synthetic control of the band gap on a single perovskite nanostructure is vitally essential for their promising prospects in studying electron-transport characteristics, offering versatile platforms for quantifying ion diffusivity and enabling efficient charge separation in optoelectronic devices.[1,33−37] So far, many perovskite heterojunction nanostructure-based photodetectors have been reported. For example, two-dimensional (2D)−three-dimensional (3D) halide perovskite $(BA)_2MA_{n-1}Pb_nBr_{3n+1}$-$MAPbBr_3$ (n = 1−3) lateral heterostructures enabled a high-performance photodetection with a responsivity and a detectivity of 4.4 A/W and 3.9×10^{13} Jones, respectively.[1] A $CsPbBr_3$−PbS p−n junction photodetector exhibited excellent performance with a responsivity of 26.9 A/W and a detectivity of 2.24×10^{11} Jones.[38] Furthermore, many nanoscale axial heterojunction nanowires have also been designed and studied. The single-crystalline $MAPbBr_3$−$MAPbBr_{3-x}I_x$ p−n junction nanowire array photodetector was reported by Guan et al. to exhibit a high responsivity of 265 A/W for a wide spectral range from 405 to 635 nm.[39] $MAPbBr_3$−$MAPbI_3$ heterostructure arrays have been reported to achieve high-performance photodetectors with a responsivity and a detectivity of 18.1 A/W and 4.41×10^{13} Jones, respectively.[40] Although these heterostructure photodetectors exhibited high photoelectric response and performance, the application of photodetectors for optical encryption communication is still hindered by challenges, such as complicated design and cumbersome operation.

Received: July 14, 2025
Revised: July 25, 2025
Accepted: July 25, 2025
Published: July 28, 2025

https://doi.org/10.1021/acs.nanolett.5c03661
Nano Lett. 2025, 25, 12091−12100

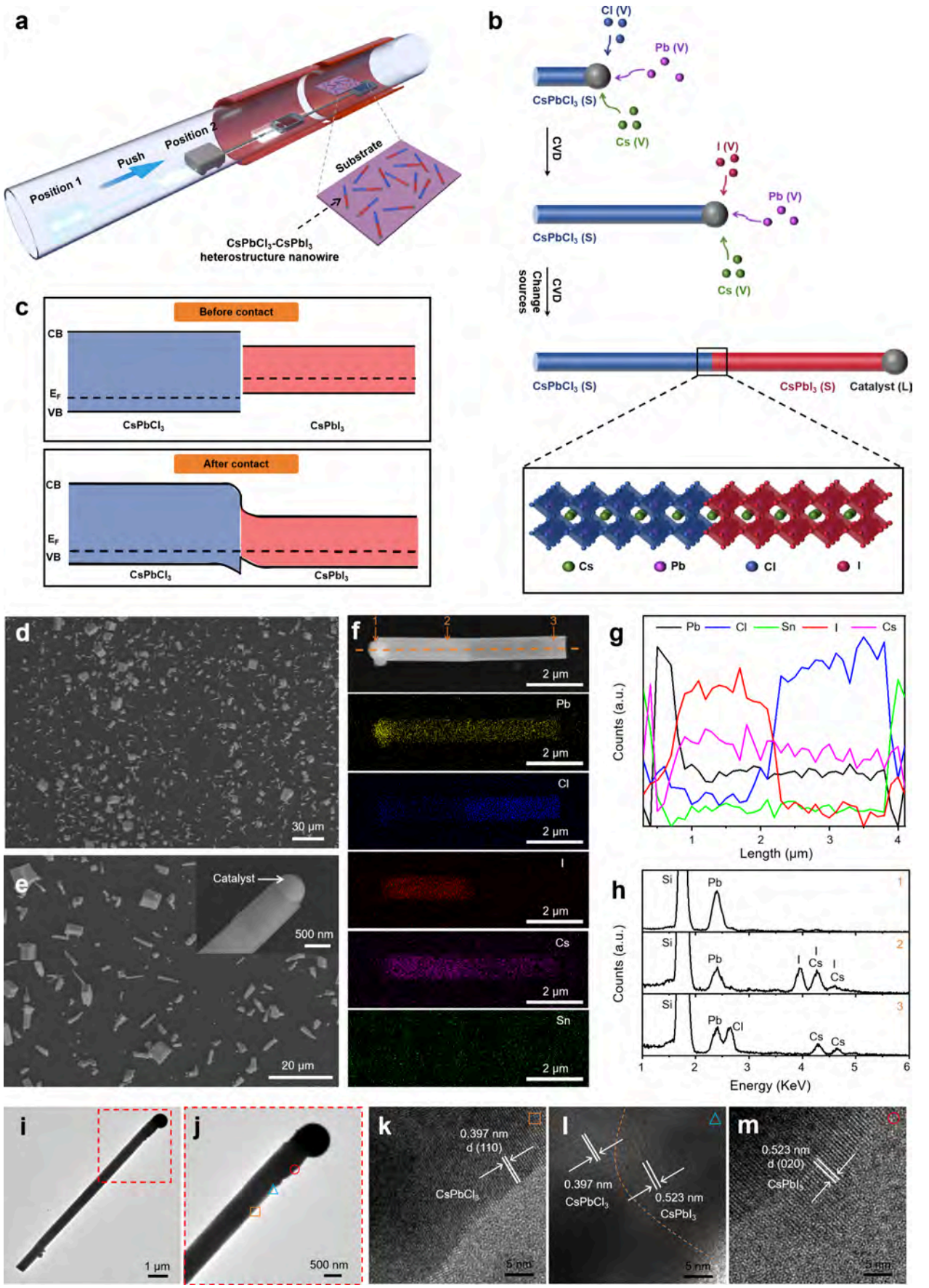

Figure 1. Fabrication process and schematic diagrams of the $CsPbCl_3$−$CsPbI_3$ heterostructure nanowires before and after contact. (a) Schematic growth diagram of the $CsPbCl_3$−$CsPbI_3$ heterostructure nanowires using a magnetic-pulling CVD system. (b) Schematic diagrams showing the

https://doi.org/10.1021/acs.nanolett.5c03661
Nano Lett. 2025, 25, 12091−12100

Figure 1. continued

fabrication process of $CsPbCl_3$−$CsPbI_3$ heterostructure nanowires and their atomic structure at the heterointerface. (c) Schematic energy band diagram of $CsPbCl_3$ and $CsPbI_3$ separately and as a heterostructure in thermal equilibrium. (d and e) Low- and high-resolution SEM images of $CsPbCl_3$−$CsPbI_3$ heterostructure nanowires. (f) SEM image and 2D EDX mapping for Pb, Cl, I, Cs, and Sn elements of a single heterostructure nanowire. (g) Line scan of a typical nanowire (dotted line shown in part f) showing the concentration profiles of different elements. (h) EDX spectra at three typical positions along the axial direction of a nanowire, as indicated in part f. (i) Low-resolution and (j) enlarged TEM images of a representative $CsPbCl_3$−$CsPbI_3$ heterostructure nanowire. (k−m) HR-TEM images of three typical positions along the heterostructure wire, as indicated in part j.

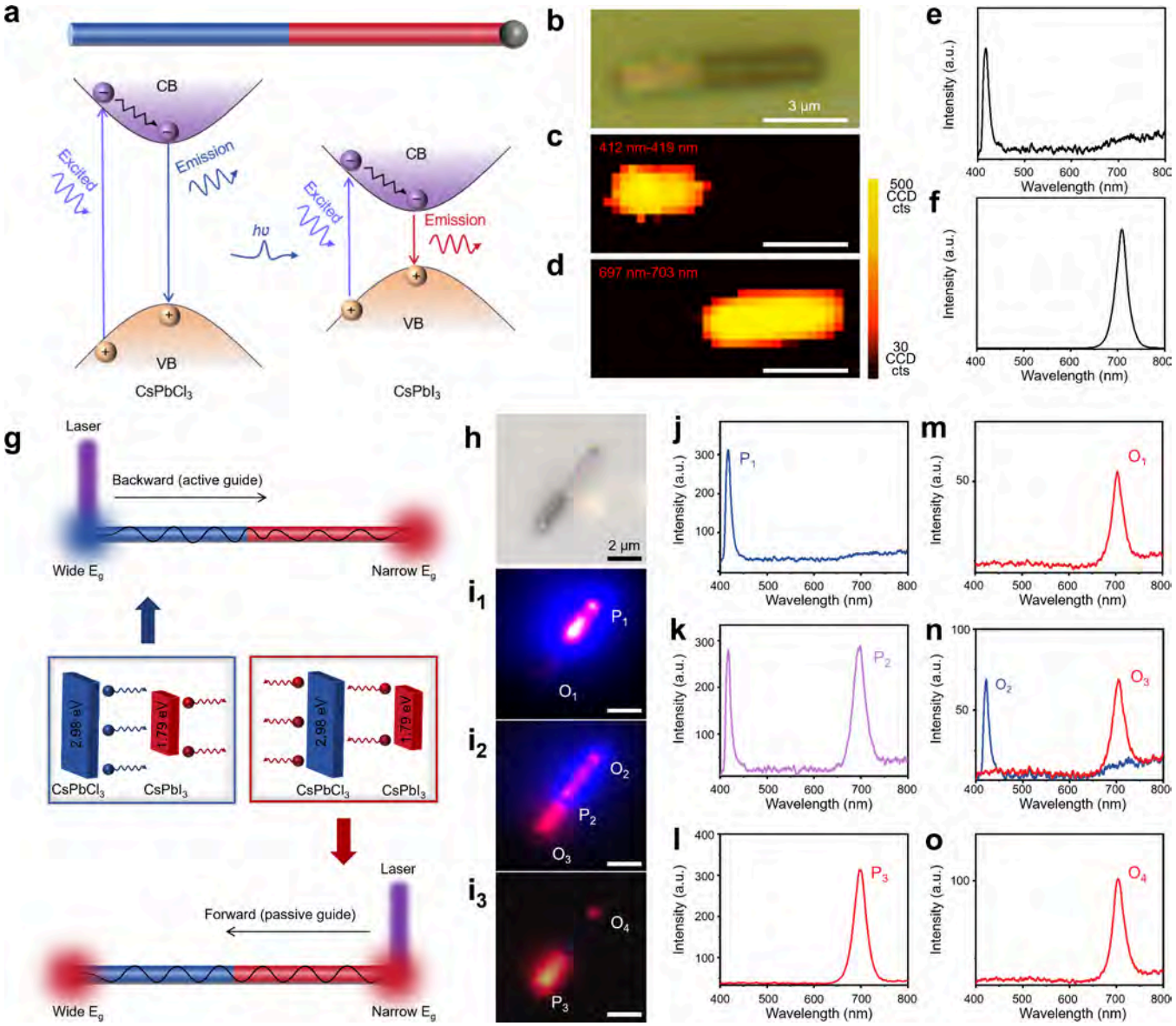

Figure 2. Room-temperature optical properties of the perovskite heterostructure nanowires. (a) Schematic illustration of the heterostructure nanowire and its corresponding energy-band diagrams and electronic excitations of a $CsPbCl_3$−$CsPbI_3$ nanowire under light illumination. (b) Representative optical image of a single heterostructure nanowire. (c−f) 2D PL mapping and corresponding PL spectra of a selected nanowire (as indicated in part b) in the emission regions of 412−419 and 697−703 nm, respectively. (g) Schematic illustrations of asymmetrical waveguides exhibiting active and passive guiding behaviors. (h) Optical image and (i) corresponding real-color images of a single heterostructure nanowire irradiated by a laser at three typical positions. (j and k) Corresponding PL spectra at the excitation position (P_1, P_2, and P_3) and PL spectra of waveguide light at output ends (O_1, O_2, O_3, and O_4) of the heterostructure nanowire, respectively.

In this work, we report on a simple synthesis strategy of perovskite heterostructure nanowires by a chemical vapor deposition (CVD) approach. Structural characterizations reveal that these nanowires have a high crystalline quality. Spatially resolved microphotoluminescence (μ-PL) spectra reveal that the nanostructures exhibit two emission bands at 417 and 698 nm, respectively, along the axial direction of the nanowires. Additionally, upon excitation with a focused laser beam, asymmetrical waveguide behavior is clearly observed on the heterostructure nanowire. Moreover, the perovskite

https://doi.org/10.1021/acs.nanolett.5c03661
Nano Lett. 2025, 25, 12091−12100

heterostructure nanowires show preeminent photodetection performance with a high responsivity of 20.58 A/W, a high detectivity of 7.52×10^{12} Jones, and reproducibility with rise and decay times of about 18.2 and 17.6 ms, respectively, which are clearly superior to photodetectors based on pure $CsPbCl_3$ nanowires. Furthermore, optical communication and encrypted imaging sensors are realized based on their unique heterostructures, paving the way for robust chiroptical data encoding and encryption mechanisms. All of these results indicate the potential of $CsPbCl_3$−$CsPbI_3$ heterostructure nanowires for multifunctional image sensors in the future.

Figure 1a shows a schematic growth diagram for $CsPbCl_3$−$CsPbI_3$ nanowires using a magnetic-pulling CVD method (Experimental Section and Figure S1). As illustrated in Figure 1b, liquid Sn catalyst (melting point of 232 °C) was supersaturated through the addition of vapor-phase precursors (Cs, Pb, and Cl), inducing the growth of $CsPbCl_3$ nanowires at the liquid−solid interface.[41,42] Consequently, high-quality $CsPbCl_3$ nanowires were obtained on the SiO_2/Si substrate through a vapor−liquid−solid (V−L−S) mechanism. Scanning electron microscopy (SEM) and energy-dispersive X-ray (EDX) analyses of $CsPbCl_3$ nanowires suggest that the atomic ratio of Cs, Pb, and Cl is close to 1:1:3 in pure $CsPbCl_3$ nanowires (Figure S2). Subsequently, the vapor sources were switched from Cs−Pb−Cl to Cs−Pb−I components using a magnetic-pulling system by a step motor. The new vapor-phase precursors were then absorbed by the catalysts, forming spatially resolved $CsPbCl_3$−$CsPbI_3$ heterostructure nanowires. A schematic atomic structure of the $CsPbCl_3$−$CsPbI_3$ heterojunction interface is shown in the inset image of Figure 1b, in which axially stacked two distinct regions ($CsPbCl_3$, blue region; $CsPbI_3$, red region) can be clearly observed. Figure 1c shows the energy band diagrams of the two perovskite materials separately and as a heterostructure in thermal equilibrium. As shown in Figure 1c, $CsPbCl_3$ and $CsPbI_3$ exhibit a type-II band offset, and their heterostructures with abrupt interfaces may promote the separation of photoexcited electrons and holes, establishing the foundation for high-performance photodetectors.[43,44]

Parts d and e of Figure 1 show low- and high-resolution SEM images of $CsPbCl_3$−$CsPbI_3$ nanowires grown on the SiO_2/Si substrate. These nanowires have a length of 5−15 μm and a diameter ranging from 0.5 to 1 μm. It is observed that a catalyst is located at the nanowire's tip (inset image in Figure 1e), indicating a V−L−S growth mechanism of the nanowires. The high-resolution SEM image and corresponding 2D EDX elemental maps of a typical $CsPbCl_3$−$CsPbI_3$ nanowire are shown in Figure 1f, indicating the uniform distribution of Cs and Pb elements along the whole nanowire. Meanwhile, the elemental maps for Cl and I reveal the spatially resolved distribution with an abrupt change across the heterointerface, indicating the successful formation of the $CsPbCl_3$−$CsPbI_3$ heterostructure nanowire. Besides, the catalyst is mainly composed of Pb. Elemental profiles (Figure 1g) along the length of a typical wire (dotted line, as indicated in Figure 1f) show the distribution of Cl and I elements along the nanowires. EDX spectra (Figure 1h) from three typical positions (points 1−3, Figure 1f) indicate that nanowires are mainly composed of Cs, Pb, and Cl or I (atomic ratio of 1:1:3) with negligible Sn contamination (Figure S3). All elemental analyses consistently reveal the formation of $CsPbCl_3$−$CsPbI_3$ heterojunctions along the axis of the nanowires.

The atomic structure and crystallinity of a representative nanowire were investigated by transmission electron microscopy (TEM), as shown in Figure 1i−m. Parts i and j of Figure 1 show low-resolution TEM images (red square in Figure 1i) of a representative $CsPbCl_3$−$CsPbI_3$ nanowire, which was transferred from the SiO_2/Si substrate to a copper microgate using a 3D mechanical arm (Figure S4). High-resolution TEM (HR-TEM) images taken from three typical positions (indicated by "□", "Δ", and "○" in Figure 1j) along the heterojunction are shown in Figure 1k−m, which display high-quality single-crystalline heterostructures with no detectable crystalline defects. The HR-TEM image from farthest from the tip (the "□" region) shows a distinct lattice spacing of 0.397 nm, corresponding to the (110) lattice spacing of the orthorhombic $CsPbCl_3$ phase. A larger lattice spacing of 0.523 nm, which can be attributed to the (020) planes of the orthorhombic phase $CsPbI_3$ is observed in the HR-TEM image taken from the "○" region. A well-defined heterointerface (orange dotted line in Figure 1l) in the HR-TEM image taken from the "Δ" region is clearly observed. Results of structural characterizations of these as-grown microstructures reveal high-quality $CsPbCl_3$−$CsPbI_3$ heterostructure nanowires with relatively abrupt interfaces at the junctions.

Low-resolution optical images shown in Figure S5 show abundant $CsPbCl_3$−$CsPbI_3$ heterostructure nanowires on the substrate. As an example, the optical properties of a representative single heterostructure nanowire (Figure 2b) using confocal optical microscopy (Figure S6) are investigated. Figure 2a shows a schematic diagram of a $CsPbCl_3$−$CsPbI_3$ heterostructure nanowire and the corresponding energy bands of $CsPbCl_3$ (2.98 eV) and $CsPbI_3$ (1.79 eV) under a focused 375 nm laser illumination. The 2D PL mapping and corresponding μ-PL spectra of a single $CsPbCl_3$−$CsPbI_3$ heterostructure nanowire exhibit two emission bands at 412−419 and 697−703 nm, as shown in parts c and d of Figure 2, respectively. The corresponding PL spectra (Figure 2e,f) clearly show that the wire has heterojunctions composed of $CsPbCl_3$ (wide-gap segment) and $CsPbI_3$ (narrow-gap segment), respectively. These images show distinct emissions from perovskites with different compositions separated by a clear boundary at the heterojunction interface.

A symmetric waveguide behavior based on a $CsPbCl_3$−$CsPbI_3$ heterostructure nanowire is illustrated schematically in Figure 2g. Figure 2h shows the optical image of a typical heterostructure nanowire with two distinct segments (dark and light, corresponding to the $CsPbCl_3$ and $CsPbI_3$ segments, respectively). The dark-field emission images (Figure 2i_1−i_3) show that the emitted light was guided by the wire cavity and leaked out at the ends of the nanowire. When excited at the wide-gap segment ($CsPbCl_3$) of the wire, the μ-PL spectra collected at the excitation (P_1) and output location (O_1) exhibit blue and red emissions at wavelengths of 417 and 703 nm (Figure 2j,m), respectively. It can be seen that the output signal (O_1) is significantly red-shifted relative to the input signal (P_1) due to reabsorption and emission processes, corresponding to the active waveguide mode (from $CsPbCl_3$ to $CsPbI_3$). Conversely, when excited at the narrow-gap segment ($CsPbI_3$; P_3), there is no obvious shift in the PL spectra (Figure 2l,o), which indicates that photons propagate through the nanowire to the end of the wide-gap segment (O_4) via total internal reflections,[45] corresponding to passive waveguiding (from $CsPbI_3$ to $CsPbCl_3$). In particular, when the laser is locally irradiated at the junction (P_2) of the wire, two emission

https://doi.org/10.1021/acs.nanolett.5c03661
Nano Lett. 2025, 25, 12091−12100

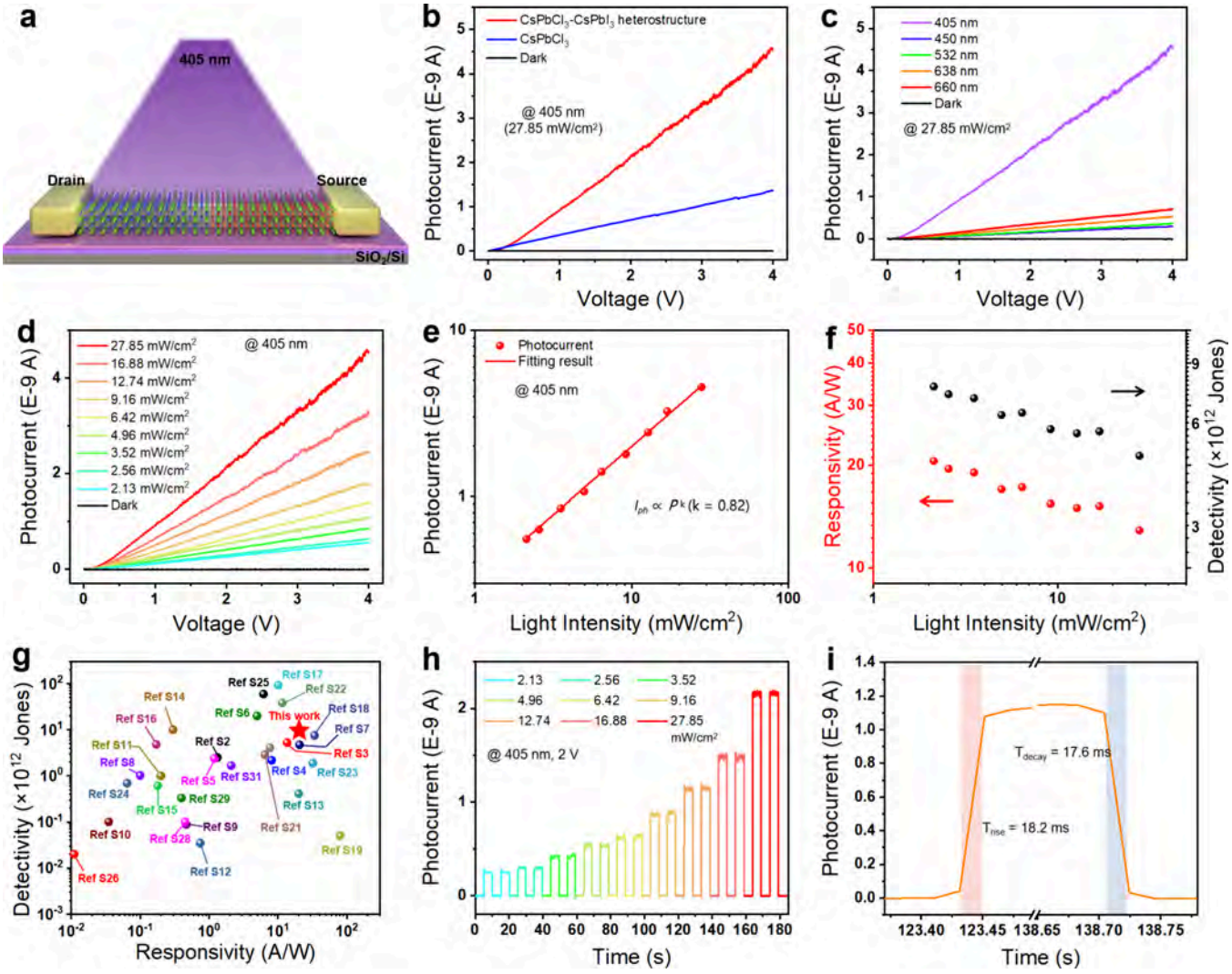

Figure 3. Optoelectronic performance of $CsPbCl_3$−$CsPbI_3$ heterostructure-nanowire-based photodetectors. (a) Schematic diagram of a heterostructure-nanowire-based photodetector. (b) I−V measurements of devices based on the $CsPbCl_3$−$CsPbI_3$ heterostructure nanowires and pure $CsPbCl_3$ nanowires under 405 nm laser illumination and in the dark. (c) I−V curves with illumination of different wavelengths (P = 27.85 mW/cm^2) and in the dark. (d) I−V curves of the photodetector illuminated under a 405 nm laser with different power densities. (e) Dependence of the photocurrent with a power intensity of 405 nm incident light at a bias of 4 V. (f) Light-intensity-dependent responsivity (red dots line) and detectivity (black dots line) of the devices based on heterostructure nanowires under a 405 nm laser illumination at a bias of 4 V. (g) Comparison of the responsivity and detectivity of photodetectors of this work with those reported in the literature. (h) Photoresponse curves for different intensities of the laser at a bias of 2 V. (i) Response time (rise and decay time) of a heterostructure nanowire photodetector under 405 nm laser illumination.

peaks at 417 and 698 nm are observed (Figure 2k), which correspond to the near-band-edge emissions of $CsPbCl_3$ (2.98 eV) and $CsPbI_3$ (1.79 eV), respectively.[46−49] The straightforward superimposition of the PL spectra at the interface implies a pronounced and abrupt junction between $CsPbCl_3$ and $CsPbI_3$ in these heterostructures. Meanwhile, the asymmetric waveguide behavior observed in Figure 2n demonstrates respective active and passive guiding toward the two ends (wide gap and narrow gap) of the wire.

To further investigate the optoelectronic performance of the $CsPbCl_3$−$CsPbI_3$ heterostructure nanowires, photodetectors based on these perovskite heterostructures were designed and fabricated. Both electrodes were deposited by using a mask with a gap of 2 μm on both ends of the wires. Meanwhile, a photodetector based on a single pure $CsPbCl_3$ nanowire with similar size (length = 2 μm; diameter = 600 nm) was constructed for comparison (Figure S7). Figure 3a shows a schematic diagram of a photodetector fabricated by using an individual $CsPbCl_3$−$CsPbI_3$ heterostructure nanowire. A comparison of the current−voltage (I_{ds}−V_{ds}) characteristics under a 405 nm laser illumination with 27.85 mW/cm^2 and in the dark for the $CsPbCl_3$−$CsPbI_3$ heterostructure nanowire and the pure $CsPbCl_3$ nanowire photodetectors is shown in Figure 3b. The results show that photocurrents from the heterostructure photodetectors (red line) are about 3 times higher than that from the pure $CsPbCl_3$ nanowire (blue line). This enhanced photocurrent in the heterostructure photodetector originates from the effective separation of photogenerated carriers due to the built-in electric field at the heterojunction (Figure S8). The I_{ds}−V_{ds} characteristics of the $CsPbCl_3$−$CsPbI_3$ heterostructure nanowire photodetectors with an excitation power of P = 27.85 mW/cm^2 at different wavelengths (λ = 405, 450, 532, 638, and 660 nm) and dark conditions are shown in Figure 3c. It is observed that

https://doi.org/10.1021/acs.nanolett.5c03661
Nano Lett. 2025, 25, 12091−12100

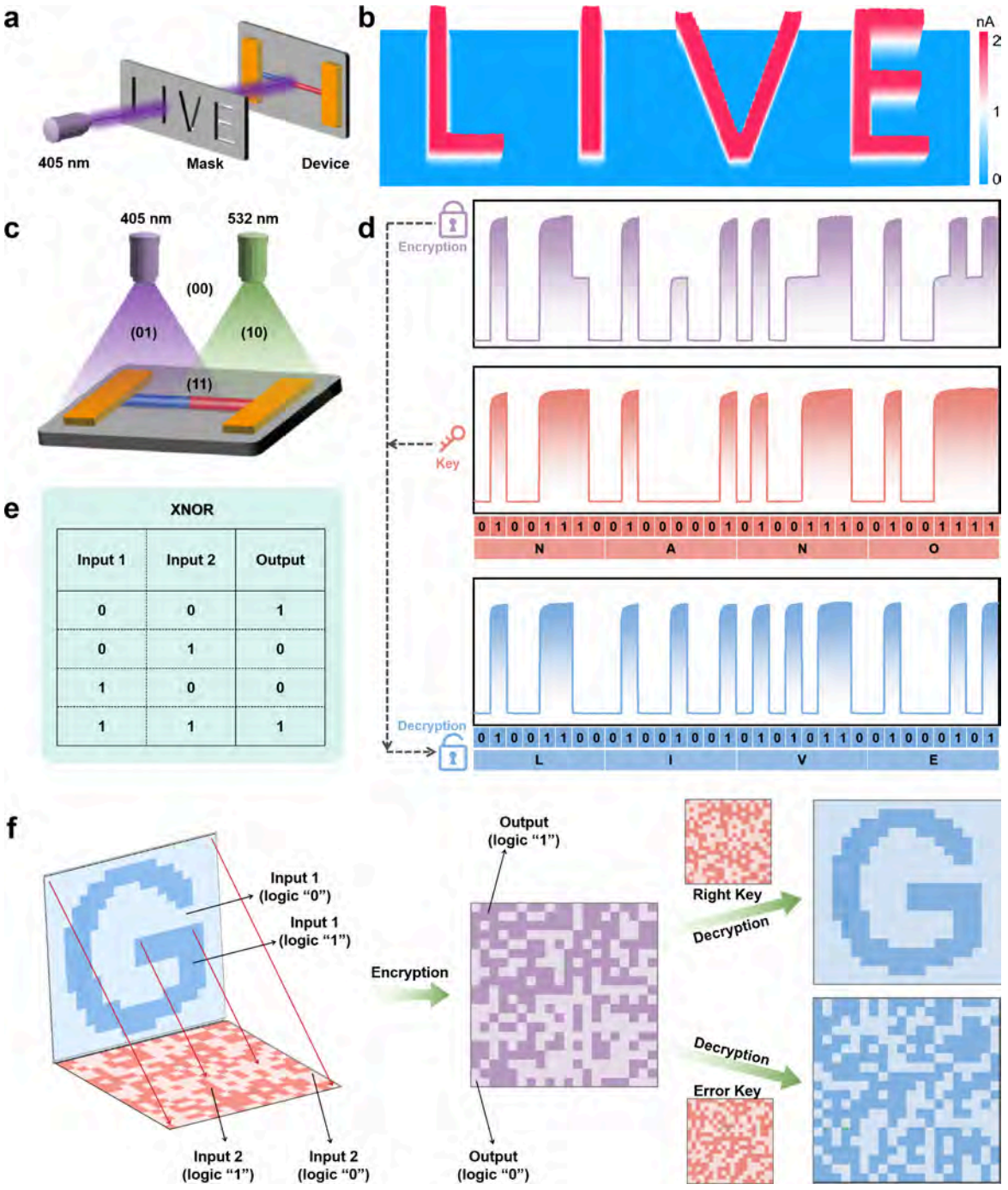

Figure 4. Optical communications and encrypted imaging applications based on the $CsPbCl_3$−$CsPbI_3$ heterostructure nanowires. (a) Schematic diagram showing imaging sensing using the heterostructure nanowire photodetector. (b) Corresponding 2D photocurrent mapping images of "LIVE" under 405 nm laser illumination. (c) Schematic diagram showing the construction of wavelength-tunable optical communications based on heterostructure nanowire devices. (d) Encrypted communication processes encoded for "LIVE". The optical signal of ASCII of the key file "NANO" is encoded. The original information "LIVE" is decrypted using the key file. (e) Truth table of logic gate "XNOR". (f) Schematic diagrams showing the encrypted image transmission process.

conductance of the heterostructure is very small in the dark (only ~10^{-12} A), while high photocurrents of 4.54×10^{-9}, 0.29×10^{-9}, 0.36×10^{-9}, 0.52×10^{-9}, and 0.70×10^{-9} A are recorded under 405, 450, 532, 638, and 660 nm laser illumination at a bias of 4 V. Under illumination with different wavelengths (P = 27.85 mW/cm^2), photocurrents increase dramatically, demonstrating high sensitivity of the heterostructure photodetector. The power-dependent I_{ds}−V_{ds} curves for the heterostructure nanowire photodetector under 405 nm laser illumination are displayed in Figure 3d, which show that the photogenerated current increases with the excitation power (P) due to an increase in the concentration of photogenerated carriers. Figure 3e reveals the dependence of photocurrent I_{ph} ($I_{ph} = I_{ds} - I_{dark}$) on the incident light intensity under 405 nm excitation at a bias of 4 V. The data in Figure 3e are fitted with the expression

https://doi.org/10.1021/acs.nanolett.5c03661
Nano Lett. 2025, 25, 12091−12100

$$I_{ph} = AP^{k} \quad (1)$$

where A is a scaling constant and k is a correlation coefficient depicting the relationship between the photocurrent and incident light power density P. The best fit of our data with eq 1 yields a k of 0.82, which suggests an almost perfect linear relationship, underscoring the heterostructure nanowire's high photoelectric conversion efficiency devoid of significant trap or energy-level interference.[50] The above results show that the prepared heterostructure nanowires are beneficial for the transport and separation of carriers, thus improving device the photoelectric conversion efficiency.[51]

The photoresponsivity (R) and detectivity (D^*) are two other important parameters to assess the performance of photodetectors. They can be given in the following expressions:

$$R = \frac{I_{ph}}{PA} \quad (2)$$

$$D^* = R\sqrt{\frac{A}{2eI_{dark}}} \quad (3)$$

where I_{ph} denotes the photocurrent, P is the light intensity, A is the effective illuminated area, and e is the electronic charge. R and D^* as a function of the excitation intensity for the heterostructure nanowire photodetector are plotted in Figure 3f. It is worth noting that both R and D^* of $CsPbCl_3$−$CsPbI_3$ heterostructure nanowire photodetectors exhibit a monotonic decrease with an increase of the incident power density (Figure 3f), which may be due to the enhanced Auger recombination rate of photogenerated carriers and the shortened carrier lifetime under a higher power density.[52,53] Under 405 nm laser illumination with a light intensity of 2.13 mW/cm^2, the device achieved a R of 20.58 A/W and a corresponding D^* of 7.52 × 10^{12} Jones, respectively. Impressively, R and D^* values of the heterostructure photodetectors are significantly higher than those of the pure $CsPbCl_3$ wires (6.11 A/W and 1.46 × 10^{12} Jones). Figure 3g and Table S1 compare the performance parameters of our heterostructure nanowire photodetector with other reported detectors.

Meanwhile, we investigate the external quantum efficiency (EQE) of the photodetector (Figure S9), which is defined as follows:

$$EQE = \frac{hcR}{e\lambda} \quad (4)$$

where R, h, c, e, and λ are the photoresponsivity, Planck's constant, speed of light, elementary charge, and wavelength of incident light, respectively. We observe that, at lower incident power densities of 2.13 mW/cm^2, the heterostructure nanowire photodetector exhibits an impressive EQE value of 6.31 × 10^3%, which is much higher than that for the pure $CsPbCl_3$ nanowire-based devices (1.87 × 10^3%), indicating high absorption efficiency and photoexcited carrier separation efficiency in the heterostructure detectors. Figure 3h shows the time-dependent current response (I_{ds}−T) of the photodetectors based on a $CsPbCl_3$−$CsPbI_3$ heterostructure nanowire at different light power intensities. The rise and decay times are 18.2 and 17.6 ms, respectively (Figure 3i), which are faster than the pure $CsPbCl_3$-based devices (34 and 42 ms) in this work (Figure S7) as well as those reported from previous studies.[54,55] Furthermore, the stability of the heterostructure nanowire photodetector is shown in Figures S10 and S11, which evidently confirm its exceptional photovoltaic response performance and operational stability.

The $CsPbCl_3$−$CsPbI_3$ heterostructure nanowire photodetector exhibits high photoresponse, responsivity, and detectivity, which is important for the application of imaging sensers, optical communications, and information encryption.[5,56] The schematic diagram of an image sensing system is illustrated in Figure 4a. A 405 nm laser served as the light source and was positioned in front of an image mask featuring a hollowed-out "LIVE" pattern. Subsequently, the photodetector generates a real-time current signal, producing a corresponding high-resolution "LIVE" image when light illuminates the $CsPbCl_3$−$CsPbI_3$ wire-based photodetectors (Figure 4b). At different X pixel points, the 405 nm laser scans along the Y direction of the mask and the time-dependent photocurrent curves of the "LIVE" pattern are displayed in Figure S12, respectively.

Additionally, Figure 4c provides a schematic diagram of the encrypted light communication system, which has been achieved by combining double-beam irradiation modes and an encryption algorithm mechanism. As illustrated in Figure 4d, two light sources with wavelengths of 405 and 532 nm are regularly tuned to on/off states, and four illumination modes of signal inputs are formed, denoted as 00, 01, 10, and 11, respectively. An encrypted optical signal is generated through superimposition of the initial and key signals by manipulating the 405 and 532 nm lasers. Then, the ASCII code of "NANO" is used as the key file to obtain the initial ASCII code by reversing the encrypted signal, recovering the original information "LIVE", and completing the decryption communication (Figure 4d). Furthermore, the capability of the device to perform secure encoded image transmission using a similar encryption protocol is demonstrated (Figure 4e,f). From the truth table (Figure 4e), an XNOR gate was designed for the encrypted imaging. Figure 4f shows that an original image signal of "G" can be transmitted and mapped onto a 20 × 20 pixel matrix, with the color of each pixel representing the logic of "0" or "1". Then, a randomly generated pixel array (20 × 20 pixels) can enable further secure encryption of sophisticated information corresponding to 2D image signals. Finally, the output image mapping could be generated according to the correspondence of the truth table as encrypted information with garbled characters, which could realize the secure encryption of the original signals. This technology can ensure that the image signals can only be decrypted using the right key sequence. Moreover, even if an interception occurs during the transmission process, the decrypted signals will not correspond to the original images, yielding a distorted and unusable reconstruction. All of these results not only highlight the potential of $CsPbCl_3$−$CsPbI_3$ heterostructure nanowire photodetectors for advanced integrated optoelectronic image sensing applications but also underscore its potential for encrypted communications in the future.

In summary, we report on the design and fabrication of on-wire $CsPbCl_3$−$CsPbI_3$ heterostructures via a modified magnetic-pulling source-moving CVD method. Structural characterizations reveal that these as-grown nanowires have heterojunctions along a single wire with abrupt interfaces. Optical properties show dual-wavelength emissions of 417 and 698 nm at the heterojunctions, suggesting abrupt heterojunctions at the interface. Moreover, photodetectors were fabricated using these $CsPbCl_3$−$CsPbI_3$ heterostructures, and

https://doi.org/10.1021/acs.nanolett.5c03661
Nano Lett. 2025, 25, 12091−12100

they exhibit an outstanding optoelectronic response over 3 times higher than that of pure $CsPbCl_3$ wires. Additionally, the heterostructure photodetector exhibits superior photodetection performance, including a high responsivity of 20.58 A/W, a detectivity of 7.52×10^{12} Jones, and a fast rise and decay time of ~18 ms. Ultimately, imaging sensing and encrypted optical communication systems are realized by the perovskite photodetectors, which makes the information transmission process more covert, more secure, and difficult to intercept and decode. This work provides a feasible and efficient approach to developing high-performance photoelectronic devices and provides a foundation for the future evolving security communications.

■ ASSOCIATED CONTENT

Supporting Information

The Supporting Information is available free of charge at https://pubs.acs.org/doi/10.1021/acs.nanolett.5c03661.

CVD setup, SEM image, and EDX spectra of the $CsPbCl_3$ nanowires, schematic diagram of the confocal microscopy system, optical images of heterostructure nanowires, optoelectronic characterization of a typical $CsPbCl_3$ nanowire, energy-transfer process at the heterointerface, and synthesis of photodetectors based on perovskite nanomaterials (PDF)

■ AUTHOR INFORMATION

Corresponding Authors

Pengfei Guo − *College of Physics and Optoelectronics, Taiyuan University of Technology, Taiyuan 030024, China*; orcid.org/0000-0002-4785-0753; Email: guopengfei@tyut.edu.cn

Xia Shen − *School of Basics, Shanxi Institute of Energy, Taiyuan 030024, China*; Email: shenxia2019@126.com

Authors

Qihang Lv − *College of Physics and Optoelectronics, Taiyuan University of Technology, Taiyuan 030024, China*

Xuyang Li − *College of Physics and Optoelectronics, Taiyuan University of Technology, Taiyuan 030024, China*

Zitong Xu − *College of Physics and Optoelectronics, Taiyuan University of Technology, Taiyuan 030024, China*

Kin Man Yu − *Department of Physics, National Sun Yat Sen University, Kaohsiung 80424, Taiwan; Materials Sciences Division, Lawrence Berkeley National Laboratory, Berkeley, California 94720, United States*; orcid.org/0000-0003-1350-9642

Johnny C. Ho − *School of Materials Science and Engineering, City University of Hong Kong, Hong Kong 999077, China*; orcid.org/0000-0003-3000-8794

Complete contact information is available at: https://pubs.acs.org/10.1021/acs.nanolett.5c03661

Author Contributions

P.G. and X.S. conceived and designed the research. Q.L. synthesized the perovskite nanowires. Q.L. performed device fabrication and electrical characterizations. Q.L. and Z.X. contributed to optical characterizations or analyses. Q.L., P.G., J.C.H., and K.M.Y. wrote the related discussions. Q.L. and X.L. participated in the SEM and TEM analyses. P.G. and X.S. cowrote the manuscript with all of the authors' input. All authors discussed the results and commented on the manuscript.

Notes

The authors declare no competing financial interest.

■ ACKNOWLEDGMENTS

The authors are grateful to the National Natural Science Foundation of China (No. 52373246). The authors acknowledge the assistance of the Instrumental Analysis Center at Taiyuan University of Technology.

■ REFERENCES

(1) Fan, X.; Hong, E.; Wang, P.; Fang, X. Controlled Growth of 2D-3D Perovskite Lateral Heterostructures for Wavelength-Tunable Light Communication. *Adv. Funct. Mater.* **2025**, *35* (7), No. 2415491.

(2) Zheng, T.; Pan, Y.; Yang, M.; Li, Z.; Zheng, Z.; Li, L.; Sun, Y.; He, Y.; Wang, Q.; Cao, T.; Huo, N.; Chen, Z.; Gao, W.; Xu, H.; Li, J. 2D Free-Standing $GeS_{1-x}Se_x$ with Composition-Tunable Bandgap for Tailored Polarimetric Optoelectronics. *Adv. Mater.* **2024**, *36* (28), No. 2313721.

(3) Han, S.; Zhu, S.; Fan, G.; Huang, X.; Zhao, G.; Shi, R.; Huang, Y.; Wu, M.; Li, J.; Guo, Y.; Gao, Y.; Zhuang, S.; Cao, F.; Yu, X.; Zhang, D. Halide Tunable Perovskite Single Crystals as Efficient Photodetector. *Adv. Funct. Mater.* **2025**, *35*, No. 2421770.

(4) Han, Y.; Jiao, S.; Zhang, X.; Rong, P.; Zhao, Y.; Jiang, D.; He, W.; Wang, D.; Gao, S.; Wang, J. Bipolar Modulation in a Self-Powered Ultra-Wide Photodetector Based on Bi_2Se_3/AlInAsSb Heterojunction for Wavelength-Sensitive Imaging and Encrypted Optical Communication. *Adv. Mater.* **2025**, *37* (7), No. 2416935.

(5) Hou, S.; Han, L.; Zhang, S.; Zhang, L.; Zhang, K.; Xiao, K.; Yang, Y.; Zhang, Y.; Wen, Y.; Mo, W.; Tan, Y.; Yao, Y.; He, J.; Tang, W.; Guo, X.; Zhu, Y.; Chen, X. On-Chip Metamaterial-Enhanced Mid-Infrared Photodetectors with Built-In Encryption Features. *Adv. Sci.* **2025**, *12* (9), No. 2415518.

(6) Xu, Z.; Han, X.; Wu, W.; Li, F.; Wang, R.; Lu, H.; Lu, Q.; Ge, B.; Cheng, N.; Li, X.; Yao, G.; Hong, H.; Liu, K.; Pan, C. Controlled on-chip fabrication of large-scale perovskite single crystal arrays for high-performance laser and photodetector integration. *Light Sci. Appl.* **2023**, *12* (1), 67.

(7) Feng, X.; Li, C.; Song, J.; He, Y.; Qu, W.; Li, W.; Guo, K.; Liu, L.; Yang, B.; Wei, H. Differential perovskite hemispherical photodetector for intelligent imaging and location tracking. *Nat. Commun.* **2024**, *15* (1), 577.

(8) Liu, Y.; Li, Y.; Sun, J.; Du, Z.; Hu, X.; Bi, J.; Liu, C.; Ai, W.; Yan, Q. Present and future of functionalized Cu current collectors for stabilizing lithium metal anodes. *Nano Res. Energy* **2023**, *2*, No. e9120048.

(9) Lian, Y.; Jia, S.; Yu, H.; Han, J.; Jiang, J.; Lan, C.; Liu, X.; Liao, Y.; Dong, X.; Wang, Y.; Gou, J.; Wu, Z.; Jiang, Y.; Wang, J. Band Alignment Semimetal Heterojunction-Based Ultrabroadband Photodetector for Noncontact Gesture Interaction with Low Latency. *Adv. Mater.* **2025**, *37* (3), No. 2404336.

(10) Quan, S.; Guo, S.; Zhao, X.; Weller, D.; Wang, X.; Li, L.; Fu, S.; Liu, R. Enhanced Photodetection Performance of $InBiSe_3/ReS_2$ Polarization-Sensitive Heterostructure Photodetectors. *Small* **2025**, *21* (1), No. 2406148.

(11) Xu, H.; Weng, Y.; Chen, K.; Wu, C.; Hu, H.; Guo, D. Ultra-Low BER Encrypted Communication Based on Self-Powered Bipolar Photoresponse Ultraviolet Photodetector. *Adv. Opt. Mater.* **2025**, *13* (4), No. 2402238.

(12) Liu, S.; Jiao, S.; Zhao, Y.; Lu, H.; Yang, S.; Wang, D.; Gao, S.; Wang, J.; Zhao, L. Bi_2O_3 Layer-Integrated, Double-Sided Responsive, Waveband-Discriminated Perovskite Photodetector for Encrypted Optical Communication. *Adv. Opt. Mater.* **2023**, *11* (21), No. 2300831.

(13) Zhao, Y.; Jiao, S.; Yang, S.; Nie, Y.; Han, Y.; He, J.; Tao, C.; Wang, D.; Gao, S.; Wang, J.; Zhao, L. High-Performance All-

Inorganic Perovskite Tandem Photodetectors With Bi_2TeO_6 Layer Enabled by Enhanced Dual Pyro-Phototronic Effect for Triple-Encryption Imaging Sensing System with Programmable Logic Gate. *Adv. Mater.* **2025**, *37* (5), No. 2414649.
(14) Chen, M.; Wu, Z.; Qiu, Z.; Peng, J.; Gao, W.; Yang, M.; Huang, L.; Yao, J.; Zhao, Y.; Zheng, Z.; Ni, Y.; Li, J. Lensless Polarimetric Imaging and Encryption Enabled by Te/$ReSe_2$ van der Waals Heterostructure Polarization-Sensitive Photodetector. *Nano Lett.* **2025**, *25* (7), 3002−3010.
(15) Bian, L.; Cao, F.; Zhao, H.; Xiang, F.; Sun, H.; Wang, M.; Li, L. Self-Powered Perovskite/Si Bipolar Response Photodetector for Visible and Near-Infrared Dual-Band Imaging and Secure Optical Communication. *Laser Photonics Rev.* **2025**, *19* (2), No. 2401331.
(16) Qiao, B.-S.; Wang, S.-Y.; Zhang, Z.-H.; Lian, Z.-D.; Zheng, Z.-Y.; Wei, Z.-P.; Li, L.; Ng, K. W.; Wang, S.-P.; Liu, Z.-B. Photosensitive Dielectric 2D Perovskite Based Photodetector for Dual Wavelength Demultiplexing. *Adv. Mater.* **2023**, *35* (21), No. 2300632.
(17) Zhao, J.; Lo, L.-W.; Yu, Z.; Wang, C. Handwriting of perovskite optoelectronic devices on diverse substrates. *Nat. Photonics* **2023**, *17* (11), 964−971.
(18) Fan, C.; Xu, X.; Yang, K.; Jiang, F.; Wang, S.; Zhang, Q. Controllable Epitaxial Growth of Core−Shell PbSe@$CsPbBr_3$ Wire Heterostructures. *Adv. Mater.* **2018**, *30* (45), No. 1804707.
(19) Wang, H.-P.; Li, S.; Liu, X.; Shi, Z.; Fang, X.; He, J.-H. Low-Dimensional Metal Halide Perovskite Photodetectors. *Adv. Mater.* **2021**, *33* (7), No. 2003309.
(20) Fu, Y.; Yuan, M.; Zhao, Y.; Dong, M.; Guo, Y.; Wang, K.; Jin, C.; Feng, J.; Wu, Y.; Jiang, L. Gradient Bandgap-Tunable Perovskite Microwire Arrays toward Flexible Color-Cognitive Devices. *Adv. Funct. Mater.* **2023**, *33* (11), No. 2214094.
(21) Yu, H.; Lian, Y.; Yang, C.; Jia, S.; Luo, W.; Yan, Z.; Han, J.; Gou, J.; Jiang, Y.; Wang, J. Bias Configurable $Se_{0.25}Te_{0.75}$/Si Photodiode Array for Multi-Channel Encrypted Communication. *Adv. Funct. Mater.* **2025**, No. 2425559.
(22) Lu, J.; Ye, Q.; Ma, C.; Zheng, Z.; Yao, J.; Yang, G. Dielectric Contrast Tailoring for Polarized Photosensitivity toward Multiplexing Optical Communications and Dynamic Encrypt Technology. *ACS Nano* **2022**, *16* (8), 12852−12865.
(23) Ke, K.; Gao, Y.; Meng, J.; He, Y.; Deng, B.; Huang, H.; Zhang, S.-W.; Zhang, K.; Xu, Z.; Li, H.; Yao, X.; Ye, Z.; Song, L.; Shu, C.; Yang, S.; Qin, N.; Fu, H. Y.; Yip, H.-L.; Kang, F.; Wei, G. High-Performance Quasi-2D Sn-Pb Perovskite Photodetectors for High-Fidelity Image Sensing and Optical Communication. *Adv. Funct. Mater.* **2025**, *35*, No. 2424340.
(24) Meng, Y.; Lan, C.; Li, F.; Yip, S.; Wei, R.; Kang, X.; Bu, X.; Dong, R.; Zhang, H.; Ho, J. C. Direct Vapor−Liquid−Solid Synthesis of All-Inorganic Perovskite Nanowires for High-Performance Electronics and Optoelectronics. *ACS Nano* **2019**, *13* (5), 6060−6070.
(25) Li, X.; Meng, Y.; Li, W.; Zhang, J.; Dang, C.; Wang, H.; Hung, S.-W.; Fan, R.; Chen, F.-R.; Zhao, S.; Ho, J. C.; Lu, Y. Multislip-enabled morphing of all-inorganic perovskites. *Nat. Mater.* **2023**, *22* (10), 1175−1181.
(26) Zhang, Y.; Parsonnet, E.; Fernandez, A.; Griffin, S. M.; Huyan, H.; Lin, C.-K.; Lei, T.; Jin, J.; Barnard, E. S.; Raja, A.; Behera, P.; Pan, X.; Ramesh, R.; Yang, P. Ferroelectricity in a semiconducting all-inorganic halide perovskite. *Sci. Adv.* **2022**, *8* (6), No. eabj5881.
(27) Meng, Y.; Zhang, Y.; Lai, Z.; Wang, W.; Wang, W.; Li, Y.; Li, D.; Xie, P.; Yin, D.; Chen, D.; Liu, C.; Yip, S.; Ho, J. C. Au-Seeded $CsPbI_3$ Nanowire Optoelectronics via Exothermic Nucleation. *Nano Lett.* **2023**, *23* (3), 812−819.
(28) Le, H. K. D.; Zhang, Y.; Behera, P.; Vailionis, A.; Phang, A.; Brinn, R. M.; Yang, P. Room-Temperature Ferroelectric Epitaxial Nanowire Arrays with Photoluminescence. *Nano Lett.* **2024**, *24* (17), 5189−5196.
(29) Lin, C.-K.; Zhang, Y.; Gao, M.; Lin, J.-A.; Le, H. K. D.; Lin, Z.; Yang, P. Controlling the Phase Transition in $CsPbI_3$ Nanowires. *Nano Lett.* **2022**, *22* (6), 2437−2443.
(30) Li, J.; Li, J.; An, M.; Yang, S.; Bao, Y.; Wang, H.; Tang, H.; Wang, H.; Fang, Y.; Qiu, J.; Bian, J.; Xu, J.; Yang, Y. Ultralong Compositional Gradient Perovskite Nanowires Fabricated by Source-Limiting Anion Exchange. *ACS Nano* **2024**, *18* (45), 30978−30986.
(31) Oksenberg, E.; Sanders, E.; Popovitz-Biro, R.; Houben, L.; Joselevich, E. Surface-Guided $CsPbBr_3$ Perovskite Nanowires on Flat and Faceted Sapphire with Size-Dependent Photoluminescence and Fast Photoconductive Response. *Nano Lett.* **2018**, *18* (1), 424−433.
(32) Qi, X.; Zhang, Y.; Ou, Q.; Ha, S. T.; Qiu, C.-W.; Zhang, H.; Cheng, Y.-B.; Xiong, Q.; Bao, Q. Photonics and Optoelectronics of 2D Metal-Halide Perovskites. *Small* **2018**, *14* (31), No. 1800682.
(33) Singh, A.; Yuan, B.; Rahman, M. H.; Yang, H.; De, A.; Park, J. Y.; Zhang, S.; Huang, L.; Mannodi-Kanakkithodi, A.; Pennycook, T. J.; Dou, L. Two-Dimensional Halide Pb-Perovskite−Double Perovskite Epitaxial Heterostructures. *J. Am. Chem. Soc.* **2023**, *145* (36), 19885−19893.
(34) Shi, E.; Yuan, B.; Shiring, S. B.; Gao, Y.; Akriti; Guo, Y.; Su, C.; Lai, M.; Yang, P.; Kong, J.; Savoie, B. M.; Yu, Y.; Dou, L. Two-dimensional halide perovskite lateral epitaxial heterostructures. *Nature* **2020**, *580* (7805), 614−620.
(35) Xia, M.; Wang, T.; Lu, Y.; Li, Y.; Li, B.; Shen, H.; Guo, Y.; Yu, Y.; Dong, J.; Dou, L.; Liu, Y.; Shi, E. Kinetic Wulff-shaped heteroepitaxy of phase-pure 2D perovskite heterostructures with deterministic slab thickness. *Nat. Synth.* **2025**, *4* (3), 380−390.
(36) Wang, Y.; Jia, C.; Fan, Z.; Lin, Z.; Lee, S.-J.; Atallah, T. L.; Caram, J. R.; Huang, Y.; Duan, X. Large-Area Synthesis and Patterning of All-Inorganic Lead Halide Perovskite Thin Films and Heterostructures. *Nano Lett.* **2021**, *21* (3), 1454−1460.
(37) Lv, Q.; Shen, X.; Li, X.; Meng, Y.; Yu, K. M.; Guo, P.; Xiao, L.; Ho, J. C.; Duan, X.; Duan, X. On-Wire Design of Axial Periodic Halide Perovskite Superlattices for High-Performance Photodetection. *ACS Nano* **2024**, *18* (27), 18022−18035.
(38) Liu, Q.; Liang, L.; Shen, H.; Li, D.; Zhou, H. Epitaxial growth of $CsPbBr_3$-PbS vertical and lateral heterostructures for visible to infrared broadband photodetection. *Nano Res.* **2021**, *14* (11), 3879−3885.
(39) Guan, Y.; Zhang, C.; Liu, Z.; Zhao, Y.; Ren, A.; Liang, J.; Hu, F.; Zhao, Y. S. Single-Crystalline Perovskite p−n Junction Nanowire Arrays for Ultrasensitive Photodetection. *Adv. Mater.* **2022**, *34* (35), No. 2203201.
(40) Xie, H.; Chen, S.; Yang, X.; Pan, Q.; Xue, T.; Zhang, Z.; Hu, Y.; Chi, J.; Cheng, L.; Chen, B.; Song, Y.; Su, M. Printed On-Chip Perovskite Heterostructure Arrays for Optical Switchable Logic Gates. *Adv. Mater.* **2024**, *36* (33), No. 2404740.
(41) Jacobsson, D.; Panciera, F.; Tersoff, J.; Reuter, M. C.; Lehmann, S.; Hofmann, S.; Dick, K. A.; Ross, F. M. Interface dynamics and crystal phase switching in GaAs nanowires. *Nature* **2016**, *531* (7594), 317−322.
(42) Wu, Y.; Yang, P. Direct Observation of Vapor−Liquid−Solid Nanowire Growth. *J. Am. Chem. Soc.* **2001**, *123* (13), 3165−3166.
(43) Jia, C.; Lin, Z.; Huang, Y.; Duan, X. Nanowire Electronics: From Nanoscale to Macroscale. *Chem. Rev.* **2019**, *119* (15), 9074−9135.
(44) Han, B.; Qiu, Q.; Tang, Y.; Lian, B.; Liu, B.; Ding, S.; Ma, S.; Luo, M.; Wang, W.; Xu, B.; Hsu, H.-Y. Manipulating Interlayer Carrier Relaxation Dynamics in Type-II Heterostructures of 2D Hybrid Perovskites Through Organic Spacer Engineering. *Adv. Funct. Mater.* **2025**, *35* (11), No. 2417167.
(45) Zhuo, M.-P.; Tao, Y.-C.; Wang, X.-D.; Wu, Y.; Chen, S.; Liao, L.-S.; Jiang, L. 2D Organic Photonics: An Asymmetric Optical Waveguide in Self-Assembled Halogen-Bonded Cocrystals. *Angew. Chem., Int. Ed.* **2018**, *57* (35), 11300−11304.
(46) Sebastian, M.; Peters, J. A.; Stoumpos, C. C.; Im, J.; Kostina, S. S.; Liu, Z.; Kanatzidis, M. G.; Freeman, A. J.; Wessels, B. W. Excitonic emissions and above-band-gap luminescence in the single-crystal perovskite semiconductors $CsPbBr_3$ and $CsPbCl_3$. *Phys. Rev. B* **2015**, *92* (23), No. 235210.
(47) Zhou, Z.; Cui, Y.; Deng, H.-X.; Huang, L.; Wei, Z.; Li, J. Modulation of electronic and optical properties in mixed halide

https://doi.org/10.1021/acs.nanolett.5c03661
Nano Lett. 2025, 25, 12091−12100

perovskites $CsPbCl_3xBr_{3(1-x)}$ and $CsPbBr_{3x}I_{3(1-x)}$. *Appl. Phys. Lett.* **2017**, *110* (11), No. 113901.
(48) Evarestov, R. A.; Kotomin, E. A.; Senocrate, A.; Kremer, R. K.; Maier, J. First-principles comparative study of perfect and defective $CsPbX_3$ (X = Br, I) crystals. *Phys. Chem. Chem. Phys.* **2020**, *22* (7), 3914−3920.
(49) Xu, F.; Wei, H.; Wu, Y.; Zhou, Y.; Li, J.; Cao, B. Nonmonotonic temperature-dependent bandgap change of $CsPbCl_3$ films induced by optical phonon scattering. *J. Lumin.* **2023**, *257*, No. 119736.
(50) Wang, W.; Wang, W.; Meng, Y.; Quan, Q.; Lai, Z.; Li, D.; Xie, P.; Yip, S.; Kang, X.; Bu, X.; Chen, D.; Liu, C.; Ho, J. C. Mixed-Dimensional Anti-ambipolar Phototransistors Based on 1D GaAsSb/2D MoS_2 Heterojunctions. *ACS Nano* **2022**, *16* (7), 11036−11048.
(51) Li, S.-X.; Xia, H.; Wang, L.; Sun, X.-C.; An, Y.; Zhu, H.; Bai, B.-F.; Sun, H.-B. Self-Powered and Flexible Photodetector with High Polarization Sensitivity Based on $MAPbBr_3$−$MAPbI_3$ Microwire Lateral Heterojunction. *Adv. Funct. Mater.* **2022**, *32* (45), No. 2206999.
(52) He, W.; Kong, L.; Yu, P.; Yang, G. Record-High Work-Function p-Type $CuBiP_2Se_6$ Atomic Layers for High-Photoresponse van der Waals Vertical Heterostructure Phototransistor. *Adv. Mater.* **2023**, *35* (14), No. 2209995.
(53) Gan, Y.; Qin, S.; Du, Q.; Zhang, Y.; Zhao, J.; Li, M.; Wang, A.; Liu, Y.; Li, S.; Dong, R.; Zhang, L.; Chen, X.; Liu, C.; Wang, W.; Wang, F. Ultrafast and Sensitive Self-Powered Photodetector Based on Graphene/Pentacene Single Crystal Heterostructure with Weak Light Detection Capacity. *Adv. Sci.* **2022**, *9* (35), No. 2204332.
(54) Wu, X.; Sun, J.; Shao, H.; Zhai, Y.; Li, L.; Chen, W.; Zhu, J.; Dong, B.; Xu, L.; Zhou, D.; Xu, W.; Song, H.; Bai, X. Self-powered UV photodetectors based on $CsPbCl_3$ nanowires enabled by the synergistic effect of acetate and lanthanide ion passivation. *Chem. Eng. J.* **2021**, *426*, No. 131310.
(55) Du, Z.; Fu, D.; Yang, T.; Fang, Z.; Liu, W.; Gao, F.; Wang, L.; Yang, Z.; Teng, J.; Zhang, H.; Yang, W. Photodetectors with ultra-high detectivity based on stabilized all-inorganic perovskite $CsPb_{0.922}Sn_{0.078}I_3$ nanobelts. *J. Mater. Chem. C* **2018**, *6* (23), 6287−6296.
(56) Zhang, J.; Hu, Z.; Yang, Q.; Sun, S.; Liu, F.; Xu, H.; Wang, X.; Zhao, Y.; Zhou, N.; Dong, G.; Zhang, H.; Yang, R.; Wang, L.; Hu, W.; Li, X. Strong Anisotropy and Giant Photothermoelectricity of 1D Alloy $Nb_3Se_{12}I$-Based Photodetector for Ultrabroadband Light-Detection and Encryption Imaging Application. *Adv. Mater.* **2025**, *37* (1), No. 2410275.

https://doi.org/10.1021/acs.nanolett.5c03661
Nano Lett. 2025, 25, 12091−12100